Investigation of the Stress-induced Microcracking Processes in Crystalline Rocks through Simultaneous Acoustic Emission and Strain Monitoring

Sana Zafar[1], Ahmadreza Hedayat[1], Omid Moradian[2]

[1]Department of Civil and Environmental Engineering, Colorado School of Mines, Golden, CO, USA
[2]Department of Earth Science, Swiss Federal Institute of Technology (ETH), Zurich, Switzerland

Key Points:

- Damage evolution was continuously observed under unconfined compression on prismatic Barre granite specimens.
- Mode of deformation observed through AE was explicitly correlated by the nonelastic component of DIC strain
- Mode of deformation obtained through AE and DIC showed a consistent near-linear correlation with increasing levels of stress.

Corresponding author: S. Zafar, `sanazafar@mymail.mines.edu`

Abstract

We performed laboratory-scale experiments on Barre granite specimen with a single pre-existing flaw to study the microscopic processes that occur during the deformation of a brittle material such as granite at different stress levels from crack initiation to the failure of the specimen. Here, we focus on the evolution of the tensile and shear cracks as a function of stress under unconfined compression. Acoustic emission technique (AET) in combination with the two dimensional (2-D) digital image correlation (DIC) technique have been used to track the changes in the source mechanisms of the registered AE events, along with the development of strains around the flaw tips of a uniaxially loaded prismatic Barre granite specimen. The parametric analysis along with the moment tensor inversion of the AE signals were used to discuss the cracking levels and the cracking mechanisms. In particular, the microcracks observed through AE monitoring prior to specimen failure were presented in terms of their spatio-temporal evolution and linked with the changes in the inelastic strain component measured through the 2D-DIC along the localized area. The mode of deformation computed from the image based strain profiles, enabled direct comparison of the nucleation, growth and interaction of the microcracks with the AE monitoring technique.

1 Introduction

Cracking processes in rocks is a complex phenomena. Discrete creation and propagation of microcrack causes the brittle failure of the rocks. Therefore an understanding of the mechanics and mechanisms involved during rock fracture plays an important role in designing civil engineering structures and different rock breaking processes such as hydraulic fracturing, drilling, and blasting etc (Z. T. Bieniawski, 1967). The microcracking processes that eventually causes the failure of a material has been studied through fracture mechanics which states that microcracks are created due to localized stress concentration caused by the presence of pre-existing flaws. Griffith (1921) satisfactorily explained that the actual stress needed to fracture a bulk material is less than the theoretical stress required to break the atomic bonds of the material, this low fracture strength is due to the presence of a large number of randomly distributed microscopic flaws in the material (Griffith, 1921; Z. Bieniawski, 1967). Similarly, McClintock and Irwin (McClintock & Irwin, 1965) showed that the material deforms inelastically before the crack propagation due to the displacement field around the tips of the pre-existing flaw known as the fracture process zone. The process zone consists of microcracks and with the increase in the load, these microcracks propagate and coalesce to form macrocracks which leads to the failure of the material (Wawersik & Fairhurst, 1970). These studies indicate that the presence of pre-existing flaw in a material acts as a stress concentrator and the growth of the microcracks particularly from these stress concentration areas causes the brittle fracture of the rock specimen (S. Peng & Johnson, 1972; Tapponnier & Brace, 1976; Kranz, 1983). Therefore, a better understanding of the cracking mechanisms involved in rock damage around a pre-existing flaw is an essential pre-requisite to predict the macroscopic failure of the rock bearing structures. Although several studies have been done on rock and rock-like specimens with an existing flaw by different researchers (Bazant & Kazemi, 1990; Fortin et al., 2009; L. Wong & Einstein, 2009; Tal et al., 2016; Li & Einstein, 2017), only limited knowledge about its fracture process under unconfined compression has been obtained.

In order to study the evolution of microcracks in stressed rock specimen various direct microstructural observation techniques such as scanning electron microscope and optical microscope have been used (Brace et al., 1966; Reches & Lockner, 1994; Kranz, 1979). Tapponier and Brace (1976) investigated the progression of damage in Westerly granite specimens using scanning electron microscopy (SEM) analysis. The cracking processes and the increase in the crack density was observed as a function of stress. In their study, the evolution of shear cracks at microscopic level was overlooked because of the low magnification of the SEM. Fredrich et al. (1989) studied the micromechanical process of the brittle to plastic transition in Carrara marble using optical and transmission electron microscopy (Fredrich et al., 1989). Zhao et al.,(1993) characterized the different stress-induced cracking mechanisms by conducting real-time SEM observations on a marble plate with an inclined pre-existing flaw (Zhao et al., 1993). They observed that the microcracks were mostly tensile in nature, with a few shear cracks (L. N. Y. Wong & Xiong, 2018). Wong and Einstien (2009) performed microscopic observations on double flawed specimen under uniaxial compression. They utilized the environmental scanning electron (ESEM) and SEM imaging techniques to study the microscopic behavior and further linked the microscopic damage to the macroscopic failure of the rock specimen. As per their observation, the coalescence between the two pre-existing flaws took place through the evolution of a number of tensile microcracks . Cheng et al. (2018) investigated the progression of damage in marble specimen containing en echelon flaws using an optical microscope. Their study investigated the development of tensile and shear cracks at the microscopic and the macroscopic scale as a function of stress (Y. Cheng & Wong, 2018). Although these techniques provided useful information about the internal microstructure of the rock material subjected to loading, they failed to provide a continuous observations of the cracking processes without pausing the load or interfering with the loading process (Chang & Lee, 2004; Paterson & Wong, 2005). Therefore, as a continuous measurement technique, acoustic emission (AE) monitoring in combination with the 2D-digital image correlation (DIC) was used in this study to analyze the damage processes in real time (Moore & Lockner, 1995; Crider, 2015; Moradian et al., 2016; Ghamgosar et al., 2017; Tarokh et al., 2017). The AE technique is considered as one of the most widely used methods for non-destructive monitoring (Guo et al., 2017; Hampton et al., 2018; Xu & Zhang, 2018; Lin et al., 2019) because of its ability to detect the dynamic motions in the material whereas most of the other methods like ultrasonic testing have the ability to detect the existing geometrical defects. The 2D-DIC is also the most extensively used non-contact optical method for displacement and strain field measurement in real-time (Pan et al., 2009; Hedayat et al., 2014; Sutton et al., 2009; Shirole et al., 2019).

Various experimental studies have been conducted over the past few years using the AE and 2D-DIC techniques in combination for the damage characterization in rocks of various geometries under different loading conditions (Lin & Labuz, 2013; Lin et al., 2014; Kao et al., 2016; Guo et al., 2017; Dong et al., 2017; J.-L. Cheng et al., 2017; Li & Einstein, 2017; Lin et al., 2019). Based on these researches, it can be concluded that both the techniques in combination have the capability of detecting the damage initiation and evolution in the rock specimen. AE detects the source location and mechanism of the AE events while DIC provides the strain field related to the deformation of the material. Hence, the combination of AE and DIC can provide a detailed evaluation of the fracturing process in rocks from microscopic to macroscopic scale. Lin and Labuz(2013), Lin et al.(2014), Zhang et al.(2015) and Lin and Labuz(2019) all adopted the above-mentioned techniques to study the fracture process zone in a three point bending test on a pre-notched rock specimen. They used the two techniques to identify the size of the fracture process zone at the tips of the notch and to distinguish the regions accommodated with the process zone and the actual crack propagation within the rock specimen. Kao et al. (2016) characterized the spalling near a free surface in laboratory experiments on rocks using AE and DIC (Kao et al., 2016). They analyzed the damage based on the AE locations and compared it with the inelastic strain measurements obtained through DIC. However, the cracking mechanism was not studied in their work. Li and Einstien, 2017 conducted four point bending experiments on a pre-notched granite specimen to observe the process zone development and crack propagation using AE and DIC techniques. Based on their observations they defined the extent of process zone and crack front. In most of these studies on rocks the major focus was to identify the damage zones based on AE source locations and the DIC strain and displacement field measurements. However the evaluation of the mode of deformation from the two techniques and their correlation has been rarely reported.

This study attempts to provide an insight into the stress-induced cracking processes involved during deformation of brittle rock specimen containing a pre-existing flaw through extending the available experimental observations. In this study, the cracking processes were monitored simultaneously with an 8 channel acoustic emission system and 2D-digital image correlation technique under unconfined compression. The experimental observation based on cumulative AE hits and cumulative AE energy helped to analyze the stress thresholds corresponding to different stages of cracking and the moment tensor analysis of the AE sources provided in-depth knowledge about the cracking processes involved during this period. The 2D-DIC strain measurement approach was used to monitor the evolution of damage in terms of the nonelastic strain component with increasing levels of stress. One of the new major finding of the present study was to obtain the mode of deformation from the DIC strain profiles and relate it with the cracking mechanisms obtained through the moment tensors of AE in real time. Independent measurements of tensile and shear deformation with increasing levels of loading from the two techniques provided a unique opportunity to correlate the changes in the cracking processes explicitly with the damage in the rock specimen.

2 Experimental Design

2.1 Material

This study for the characterization of the damage process was performed on Barre granite (BG) specimen with a single pre-existing flaw. BG is crystalline in nature and obtained from the south-west region of Burlington, Vermont (USA) (Nasseri et al., 2010; Iqbal & Mohanty, 2007). This rock is a representative of the Earth's crust and one of the most extensively studied rocks with a rich literature (e.g.,(Goldsmith et al., 1976; S. S. Peng, 1975; Kranz, 1979; Morgan et al., 2013; Moradian et al., 2016)). BG is a gray granodiorite with its grain size ranging from 0.2mm to 3.0mm (medium-fine grained). It has an average grain size of 0.87mm (Nasseri et al., 2010; Iqbal & Mohanty, 2007). BG has a very consistent mineral composition which consists of about 65% felspar (average grain size of 0.95), 27% quartz (average grain size of 0.94mm), 9% biotite (average grain size of 0.83mm) (Iqbal & Mohanty, 2007; Nasseri et al., 2010; Dai & Xia, 2010) . It has a density of 2.66 gm/$cm^3$with a porosity of 0.59% (Iqbal & Mohanty, 2007). Barre granite specimen in its intact form has the following average properties: Young's modulus=58 GPa (Shirole, Walton, & Hedayat, 2020), uniaxial compressive strength=170 MPa (Zafar et al., 2020), average compressional P- wave velocity= 4000 m/s (Moradian et al., 2016). Same block of Barre granite was used to prepare the prismatic specimens (152 mm x 76 mm x 25 mm) and the pre-existing flaws were cut by OMAX water jet. The flaw was cut throughout the thickness of the specimen. The flaw length and the its inclination angle with respect to the horizontal axis is 25mm and 45°, respectively (Figure 1a). For the purpose of experimental result presentation, three representative specimens labelled as 'BG-1', 'BG-2' and 'BG-3' are discussed in this paper from a comprehensive series of tests.

2.2 Loading System Set-up

A computer-controlled servo-hydraulic loading machine was used for conducting unconfined compression experiments on three Barre granite specimen with an existing flaw. The loading was applied in displacement controlled mode at a displacement rate of 1 μm/s. The displacement was controlled through three Linear Variable Differential Transformers (LVDTs). These LVDTs recorded the overall axial deformation of the rock specimen. The displacement control mode helped in controlling the deformation of the rock specimen closed to their uniaxial compressive strength to protect the AE sensors from damage. Proper synchronization was ensured among the three systems during the test.

2.3 2D-DIC Setup

Digital image correlation (DIC) technique is the most commonly used and widely accepted non-destructive, non-contacting optical deformation and strain measurement approach that can be utilized for the evaluation of the complex behavior of geomaterials (Pan et al., 2009; Hedayat et al., 2014; Sutton et al., 2009; Bruck et al., 1989). This technique evaluates full-field displacement and full-field strains to sub-pixel accuracy by comparing the reference image (without mechanical loading) to the image corresponding to strained state (under mechanical loading). Because of its sub-pixel resolution, accurate DIC measurements detect optically invisible cracks. The 2D-DIC technique is preferred over other optical methods because of its simple experimental set-up and specimen preparation and also provides accurate displacement and strain field measurement (Hedayat & Walton, 2017).

In 2D-DIC, the image taken before applying the load is known as the reference image and this reference image is then used for comparing the images acquired throughout the loading. In order to compare the images acquired in the stressed state with the reference image, the specimen surface should have a unique random gray intensity pattern. After acquiring the digital images, DIC uses a correlation function between the images, to compare the acquired image with the reference image. An area of interest (AOI) is first specified within the image and further divided into small group of pixels known as subsets (Schwartz et al., 2013). These subsets are separated from each other through the step size. In 2D-DIC, the correlation functions such as zero normalized cross-correlation (ZNCCD) or zero normalized sum of squared difference (ZNSSD) (Pan et al., 2009) is used for tracking the subsets between the reference and the deformed images. The reason behind the selection of a square subset over a single pixel is that it provides a wider variation in the intensity of the gray scale values which makes it more identifiable from other subsets in the deformed image. To get the accurate measurement in 2D-DIC and to track the changes in the reference and the deformed images, each subset is defined by a unique distribution of gray-scale values known as the speckle pattern. The 2D-DIC technique locates the subsets in the deformed image, initially defined in the reference image assuming that the gray-scale values in the subset remains preserved even after the deformation (Bourcier et al., 2013). A correlation algorithm is then implemented between the subsets of the reference and the deformed images to find the optimal matching between the coordinates. The coordinates of the extremum position of the correlation coefficient defines the new position of the deformed subset with respect to the reference subset. The difference between the position of the reference subset and the deformed subset gives the displacement vector (Hedayat et al., 2014). The procedure is then repeated for all the virtual grid lines in a systematic manner to obtain the displacement along the surface of the specimen at various stages of deformations. The numerical differentiation of the displacement field along the specimen surface gives the strain field measurement in real time. The strain field calculation is based on the standard Lagrangian approach of the continuum mechanics. The strains around the grid points are averaged across an area (filter size) to get a continuous strain profile along the surface of the specimen.

The proper implementation of the DIC technique comprises of three consecutive steps: (i) specimen preparation and experimental set-up, (ii) image acquisition, and (iii) processing the acquired images using correlation algorithm. To obtain a high-quality gray-scale distribution for accurate DIC measurements, the planar surface of the specimen was cleaned and a unique random speckle pattern was created by using a multi-color paint (Rust-Oleum) to paint the surface of the specimen (Sutton et al., 2009).

Grasshopper (Point Grey) charged coupled device (CCD) camera with a Fujinon lens of focal length 35mm was used for acquiring the digital images. The aperture, focus and polarization of the lens were operated manually. The Fly Capture SDK software was used to control the field of view from the camera, brightness, and the rate of image acquisition (Shirole et al., 2019). Before each test, dust on the polarizing lens and reflections on the surface specimen were minimized. In our experimental setup, the CCD camera was kept at a distance of 1000 mm from the planar surface of the specimen to avoid the error due to

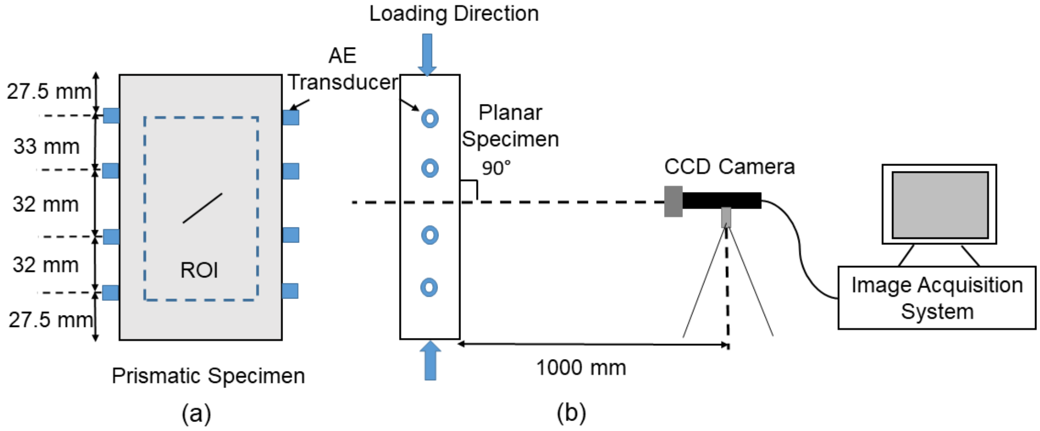

Figure 1. Schematic diagram of the (a) Prismatic specimen with a pre-existing flaw (flaw length is 25mm and the flaw inclination angle with respect to the horizontal axis is 45°) with the location of the AE sensors, the dashed blue line shows the region of interest, (B) 2D-DIC setup with the CCD camera and the image acquisition system

the out of plane deformations below the prescribed limit of $\Delta z/zc \sim 10^{-4}$ (Modiriasari et al., 2017). The surface of the specimen was kept perpendicular to the optical axis of the camera and the plane of the camera parallel to the planar surface of the specimen. The images were captured at a rate of 10 frames per second for these experiments. A polarizing lens with a conjugate polarizer was used for better illumination. The DIC component of the setup is shown in Figure 1. The whole surface (152 x 76 mm^2) of the specimen was imaged with the camera.

The digital images captured during the experiments were analyzed using the VIC-2D software licensed by Correlated Solutions to extract the displacement and strain along the specimen surface using the correlation criterion. The analysis in the software requires the selection of the appropriate region of interest (ROI) in the reference image (Figure 1). For DIC measurements a virtual grid is formed on the reference image, which requires subset size and step size as an input to the software. According to previous research, (Hedayat et al., 2014; Shirole et al., 2019), a step size of 5 pixels and a subset size of 15 pixels were selected. This provided sufficient overlap between the subsets and required less computation time for the image analysis. The correlation procedure was executed by applying a constant magnification factor to convert the pixels to their respective physical dimensions (Hedayat et al., 2014; Shirole et al., 2019). In these experiments, by comparing the pixel measurements from the fixed field of view of the camera to the physical dimension of the entire specimen surface, a constant magnification factor of $90\mu m$/pixel was used that is each pixel in the digital image is equal to $90\mu m$ in the physical dimension.

2.4 AE Setup

Acoustic Emission (AE) was implemented to track the spatiotemporal changes in the registered AE events around the flaw tips of the uniaxially loaded prismatic specimen. The experiment was instrumented with eight piezoelectric AE sensors mounted on the sides of the specimen (Figure 1a). The piezoelectric sensors Nano 30 from Mistras Group, Inc. were used in the study to record the AE signals. The Nano-30 AE sensor has a frequency response over the range of 125-750kHz with a resonant frequency of 300kHz. The miniature size of the sensor makes it easy to mount in small and tight spaces. They were attached on the sides along the longitudinal axis of the specimen with epoxy (produced by Hardman, Royal Adhesives and Sealants). The epoxy was in contact with the sensor for 9 hours and the velocity measured by Pencil Lead Break test was documented after every 1.5 hour interval. The efficiency of the coupling was verified by the pencil lead break (PLB) and the auto sensor test (AST).

In this experimental-setup, 2/4/6 PAC preamplifiers were used to amplify the output voltage of the AE sensors by 20dB in order to improve the detection efficiency of the sensors for recording. The sampling frequency was 5 MHz with a sample length of 15k and a pre-trigger of 256μs. Eight channel board and system from the MISTRAS Group, Inc. was used as a part of the AE data acquisition system. The system was controlled by real-time operating software AEwin where the peak definition time (PDT), hit definition time (HDT) and hit lockout time (HLT) were set as 200, 800 and 350 μs, respectively. The maximum duration was taken as 3ms.

All the AE signals (waveforms) were recorded and further analyzed for the source localization and source type characterization using the moment tensor inversion method reported in Li et al.(2019)(Li et al., 2019). The source location was based on the first arrival of the P-waves. The arrival time picking was done using the Akaike information criterion (AIC) (Maeda, 1985; Kurz et al., 2005). Locations were determined using a constant P-wave velocity field model for a minimum distance error of 3 mm and optimized using "fmincon" function in MATLAB. While AE source location analysis helped to describe the spatiotemporal evolution of damage, AE source mechanism analysis and their dependence on the stress state of rocks enables detailed insight into the cracking processes at the microlevel.

A generalized relationship between the seismic sources and the elastic waves is summarized by (Richards & Aki, 1980; Ohtsu, 1991). Thus, the AE waves can be represented by

$$u_{ix,t} = G_{ip,q}(x, y, t)m_{pq} * S(t) \tag{1}$$

where $u_{ix,t}$ is the displacement at crack location x, $G_{ip,q}$ (x,y,t) is the spatial derivative of Green's function, which describes the response of the medium to a disturbance, m is the moment tensor, the asterisk denotes the convolution operation and S(t) represents the source time function. The moment tensor inversion analysis based on Simplified Green's function for Moment tensor Analysis (SiGMA) procedure (Ohtsu, 1995) was used to identify the source mechanism and their evolution in these experiments. This method selects the compressional (P) wave portion from the full-space Green's function when applied to an isotropic and homogeneous material. It is a quantitative approach in which the source is represented by a moment tensor matrix (m) (Eq. 1) which is a 3x3 matrix. The elements of the matrix describes the forces acting on the source (Graham et al., 2010). Each element in the matrix denotes one of the 9 double-couples acting at the source. Since the matrix is symmetric, it contains six independent elements. The diagonal elements represent tensile or compressional couples and the off diagonal elements represent the shear couples. The SiGMA procedure uses the simplified form of Eq.(1) to determine the six independent components of the moment tensor by solving a set of linear equations in terms of the first motion amplitude A(x) as shown in Eq.(2), as follows:

$$\mathtt{A}(x) = \frac{C_s Re(t, r)}{R} \begin{bmatrix} r_1 & r_2 & r_3 \end{bmatrix} \begin{bmatrix} m_{11} & m_{12} & m_{13} \\ m_{21} & m_{22} & m_{23} \\ m_{31} & m_{32} & m_{33} \end{bmatrix} \begin{bmatrix} r_1 \\ r_2 \\ r_3 \end{bmatrix} \tag{2}$$

where A(x) is the amplitude of the first motion observed at the sensor location x. C_s is the coefficient of calibration for the sensor, R is the distance from the sensor to the AE source. Vector r is the direction vector of R and Re(t,r) denotes the reflection coefficient (Ohtsu, 1995). These values can be obtained through the source localization. Thus, source location is required to perform the moment tensor analysis.

Once the moment tensor of a source has been determined, the cracking mechanism is classified using the eigenvalues of the moment tensor (Ohtsu, 1991). The moment tensor is decomposed to its eigenvalues to split the tensor into an isotropic component (ISO), a deviatoric component 'Compensated Linear Vector Dipole' (CLVD) and a double-couple (DC) component. X and Y denotes the maximum shear and CLVD components respectively, giving a DC part (X,0,-X), a CLVD part (Y,-0.5Y,-0.5Y) and the isotropic part in direction, Z. The values of X,Y and Z calculated from the following equations are used to determine the shear and tensile crack ratios:

$$\begin{aligned} \frac{\lambda_1}{\lambda_1} &= X + Y + Z \\ \frac{\lambda_2}{\lambda_1} &= 0 - \frac{Y}{2} + Z \\ \frac{\lambda_3}{\lambda_1} &= -X - \frac{Y}{2} + Z \end{aligned} \tag{3}$$

where λ_1, λ_2 and λ_3 are the maximum, intermediate and minimum eigenvalues. In the SiGMA procedure, the values of X, Y and Z gives the shear, deviatoric and isotropic component of the source, respectively. An AE source with X $<$ 40% and Y+Z $>$ 60% is classified as a tensile crack, X $<$ 40% is typically considered as a shear crack and 40% $<$ X $<$ 60% is classified as a mixed mode crack (Ohtsu, 1995).

From the eigenvalue analysis of the moment tensor, three eigenvectors e1, e2, e3 can also be obtained. The eigenvector analysis of the moment tensor provides the orientation of the cracks. l and n represents the cracking motion vector and the vector normal to the crack surfaces which can be evaluated using equation (4):

$$\begin{aligned} e1 &= l + n \\ e2 &= l \times n \\ e3 &= l - n \end{aligned} \tag{4}$$

In case of a tensile crack, the cracking motion vector l is parallel to the normal vector n and for shear cracks the two vectors are usually perpendicular.

In this study, the above procedure was used not only to classify the different AE events as shear, tensile, or mixed mode crack but also to identify their orientation at different levels of cracking. As for the source localization in three dimensions, there are four unknowns (x, y, z, and t) which require the detection of the AE signals by minimum of four channels but the moment tensor has six independent components. Hence, in these experiments, the source localization was also done for a minimum of six channels.

3 Results and Discussion

3.1 Crack Initiation (CI) and Crack Damage (CD)

Brittle rock is a heterogeneous material made up of various inherent microstructures. Numerous experimental results demonstrate that the microcracking in rock is effected by these internal heterogeneities (Brace et al., 1966; Martin & Chandler, 1994; Eberhardt et al., 1998). Considering the fact that Barre granite is a brittle rock (quartz content is 27%) and hence the failure is caused by the initiation, growth and coalescence of microcracks created due to material heterogeneity under compression. Direct observation of these microcracks have revealed that the primary mechanism of deformation in brittle rocks is local tensile cracking which is due to the extensile strains (Lajtai, 1974; Tapponnier & Brace, 1976; Kranz, 1983; Moore & Lockner, 1995), in which the cracks are oriented parallel to the direction of the major principal stress (Wulff et al., 1999; Martin & Chandler, 1994; Moore

& Lockner, 1995). As the load applied to the specimen increases, a complex heterogeneous combination of tensile and shear stresses gets concentrated at the tips of the pre-existing flaws. Various experimental studies reveal that brittle fracture in compression is due to the development of the extensile microstresses. The macroscopic failure takes place due to the interaction of these tensile microcracks close to the tips of the pre-existing flaws. However, tensile cracks are not solely responsible for the overall failure of the material (Lajtai, 1974). Therefore, shear failure mechanism caused by the compressive stress concentration becomes active at later stages of the cracking process (Griffith, 1921; Lajtai, 1974). Once sufficient number of extensile cracks are formed, they start to interact, at this stage (crack damage stress threshold) the shear (frictional) cracking becomes dominant (Brace et al., 1966; Tapponnier & Brace, 1976; Martin & Chandler, 1994; Hajiabdolmajid et al., 2002; Jian-po et al., 2015). Martin and Chandler (1994) studied that the rock strength is made up of two components: friction and cohesion. The cohesive component is the primary strength component at early stages of loading and gets destroyed by the tensile cracking. Once sufficient damage has accumulated, the cohesion strength gets reduced and frictional strength component gets mobilized (Hajiabdolmajid et al., 2002). During this stage, high structural changes to the specimen takes place, with an increase in the density of microcracks by about sevenfold (Hallbauer et al., 1973).

The procedure adopted in this study for the quantification of the tensile and shear cracks accumulated in the rock specimen throughout the loading are described in the subsequent sections. The section deals with the cracking levels and the cracking mechanisms obtained through the experimental observations, it further illustrates the methodology used for the selection of the strain metrics evaluated from the 2D-DIC strain measurements to quantify the nonelastic damage into the rock specimen.

3.1.1 Observation of Crack Initiation (CI) and Crack Damage (CD) using AE Signatures

As shown in Figure 2 (a & b), AE signatures were observed around the flaw tips in the specified region of interest, in sync with the 2D-DIC measurements. Several studies revealed that the AE hits acquired throughout the loading corresponds to the increasing number of microcracks and the energy of the signal denotes the magnitude of the cracking sources in materials (Lockner, 1993; Moradian et al., 2016). Therefore, to investigate the cracking levels, common parametric features of the AE waveform such as hits and energy emitted by the seismic sources were analyzed as a function of the normalized stress. The two important components in the brittle rock fracture that is crack initiation (CI) and crack damage (CD) thresholds were identified (Eberhardt et al., 1998).

Figure 2 (a & b) shows the rate and cumulative plots of the AE hits and AE energy as a function of applied stress normalized by the peak strength. The trend of the changes in the cumulative plots of AE hits due to increasing level of stress are consistent for all the specimen in the region of interest. Figure 2a shows that the initiation of significant AE activity in the cumulative hits plot occurred at 37-41% of the peak strength. This behavior has been detected in all the three rock specimen. Therefore, this point can be linked as the crack initiation point among the cracking levels. This cracking level detected by AE monitoring is consistent with the findings of several other studies corroborating it as the crack initiation (Pestman & Van Munster, 1996; Nicksiar & Martin, 2013). However, cumulative AE energy plot (Figure 2b) does not show any significant change in the trend at this stage (CI), which is consistent with the fact that microcracks have very low AE energy (Kim et al., 2015). When the load is further increased beyond crack initiation, it does not lead to the failure but the cracks become stable after propagating to some fraction of its initial length, known as the stable growth of the cracks. This can be seen by the constant increase in the cumulative hits plot. The cumulative AE energy plot is also constant and does not show any significant change in this region. This constant increase in the AE signal parameters indicate 'stable crack growth.' When the load reaches 85-90% of

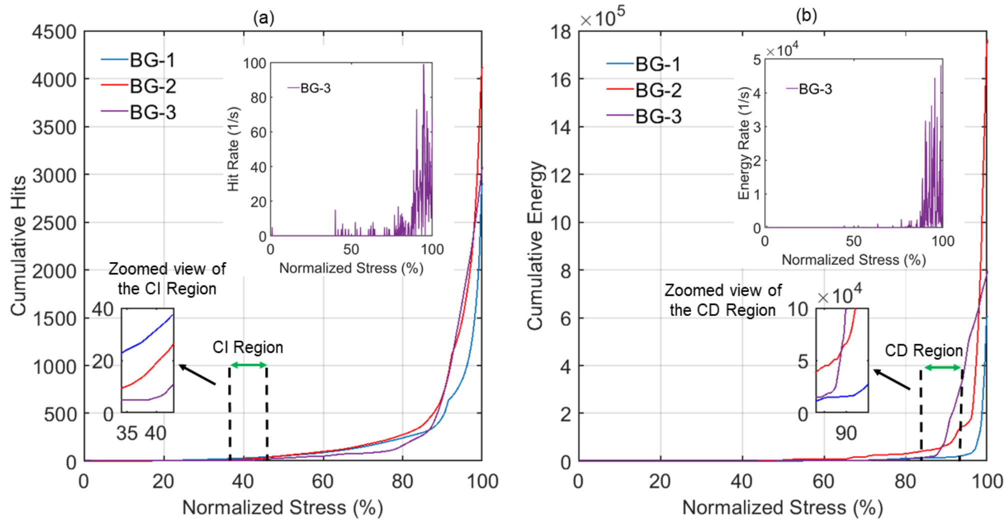

Figure 2. (a) Variation of cumulative AE hits as a function of normalized stress for the rock specimens BG-1,BG-2 and BG-3 at the specified ROI. The insets show the zoomed view of the CI region and the variation in the hit rate throughout loading for BG-3,(b) Variation of cumulative AE energy as a function of normalized stress for the rock specimen BG-1,BG-2 and BG-3 at the specified ROI. The insets show the zoomed view of the CD region and the variation of the energy rate throughout loading for BG-3.

the peak strength, the cumulative plots of AE hit and AE energy shows a sharp increase. This indicates the accumulation of microcracks to macrocracks, which is confirmed by the high amount of AE energy released at this stage. Therefore, the rise in the AE energy release can be called as 'macro-crack initiation'. Other researchers (Eberhardt et al., 1998; M. Diederichs, 2003; Nicksiar & Martin, 2012) have called this point as the 'crack damage'. At low levels of loading (0-30% of the failure stress), the AE parameters does not show any activity, whereas it has been found in previous studies that some AE signals can be seen in the initial loading stages due to crack closure and elastic deformation (Scholz, 1968; Eberhardt et al., 1998; Moradian et al., 2016). However, in these experiments, the analysis was mainly focused from the microcrack initiation to the failure of the sample, so the levels prior to the crack initiation was adopted to be quiet by setting a high threshold in the AE settings ($\sim$ 70 dB). Analysis of the digital images also did not reveal any significant information about the stages prior to crack initiation.

3.1.2 Observation of Crack Initiation (CI) and Crack Damage (CD) using 2D-DIC

The 2D-DIC technique was used to measure the strain along the specimen surface in the region of interest (ROI) and the damage was characterized based on the non-elastic strain measurements. The evolution of the non-elastic strain components in the rock specimen represents the initiation and growth of the microcracks. Therefore, in the present study, the inelastic components of the tensile and shear strain values were evaluated at various levels of loading for the analysis of the different mode of deformation.

3.1.3 Crack Initiation (CI) using Tensile Strain Measurements

As the damage progresses, strain accumulation takes place in the specimen. When the specimen is loaded under unconfined compression, major principal strain (ϵ_{11}) is caused along the longitudinal axis of the specimen, while the minor principal strain (ϵ_{22}) results due to the material expanding in the lateral direction (Poisson's effect). Based on the fact that the concentration of the local tensile stress at the tip of the flaw is the primary mode of deformation in brittle rocks (Moore & Lockner, 1995), the minor principal strain (ϵ_{22}) (extensile strain) distribution was studied in the specific region of interest for the three rock specimen to understand the effect of heterogeneity on the microcracking behavior. At low levels of loading (20% of the failure stress), the strain distribution showed a small standard deviation (0.4 mϵ). As the stress level increases, the spread in the histogram and the standard deviation also increases. At 60% of the failure stress the standard deviation in strain distribution is around 1.1 mϵ and goes upto 3 mϵ at 95% of the failure stress. This indicates the increased heterogeneity in the strain field due to strain localization at higher levels of damage. As the stress level increases the histogram shift towards the left which shows the higher concentration of the extensile strains. The spread in the histogram also indicates the increase in the number of DIC grid points with higher magnitudes of the tensile strain. As shown in Figure 3 some of the DIC grid points show compressive strain in the tensile strain field which can be due to the heterogeneous distribution of strain at the pixel scale (M. S. Diederichs, 1999; Shirole et al., 2019).

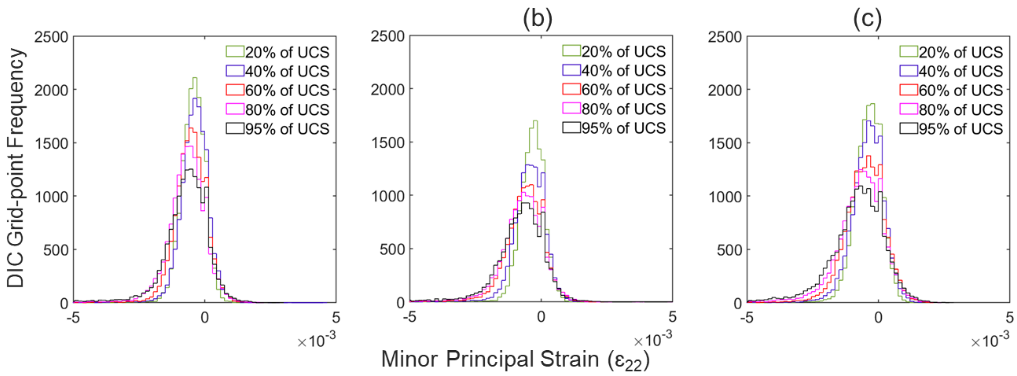

Figure 3. Histograms showing the minor principal strain distribution in the ROI for three prismatic Barre granite specimens: (a) BG-1,(b) BG-2,(c) BG-3. Negative (-) strains represent extension

In order to obtain the distribution of the localized tensile strain in the ROI, an apparent tensile strain (ϵ^T_{AT}), similar to the method adopted by (Song et al., 2013; Shirole et al., 2019), is used:

$$\epsilon^T_{AT} = \left| \sum_{i=1}^{N} \langle \epsilon_{22,i} \rangle \right| \tag{5}$$

where $\epsilon_{22,i}$ represents the minor principal strain at the ith DIC grid point, and N is the total number of DIC grid points in the specified region of interest. For the computation of the apparent tensile strain, only negative strain values are taken into account. This apparent tensile strain contains both the elastic and inelastic component of the tensile strain present in the rock specimen.

As it is known that acoustic emission is released due to microcracking which leads to the irreversible increase in the rock volume, known as dilatancy. This increase in volume is

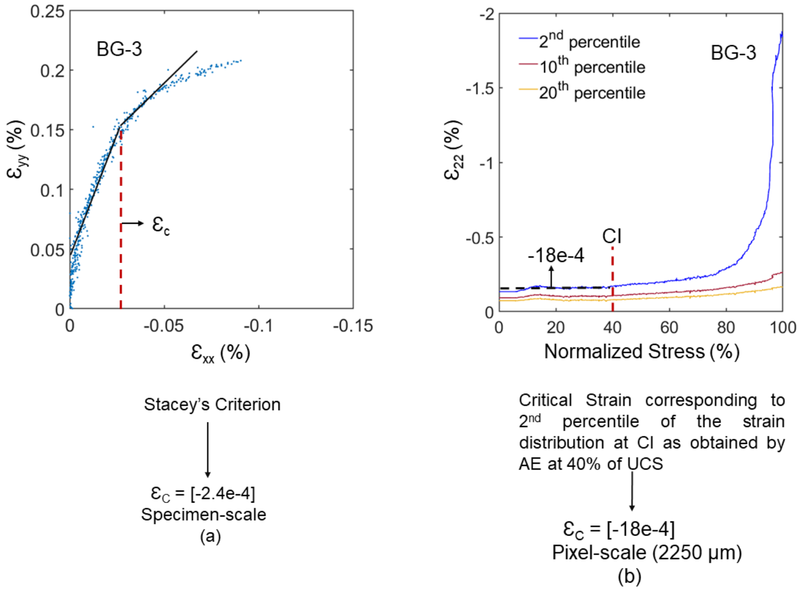

Figure 4. Procedure adopted for the evaluation of the critical threshold of tensile strain (ϵ_c) from DIC strain measurement (a) at specimen-scale (Stacey, 1981), (b) at pixel-scale (M. S. Diederichs, 1999; Shirole et al., 2019)

caused by the tensile opening. (Brace et al., 1966; Scholz, 1968; Sondergeld & Estey, 1982). Several experimental studies have shown that the initiation of the microcracking can be seen by a significant rise in the AE activity which is considered as the crack initiation stress (CI) (Eberhardt et al., 1999; Moradian et al., 2016) as shown in Figure 2. Similarly, the regions accumulated with the tensile microcracking are expected to be characterized by the tensile strain above some threshold limit at which the cracking initiates i.e. the plastic deformation takes place. With this in mind, and to establish the correlation between the microcracking observed through AE and DIC strain measurements, it is important to compute the nonelastic strain component which governs the plastic deformation in the rock specimen. To evaluate the nonelastic component, the critical tensile strain limit for Barre granite was estimated. The procedure adopted for the critical strain limit calculation is shown in Figure 4.

Due to the heterogeneous nature of rocks, the scale of strain measurement is also considered in order to calculate the critical threshold value of the tensile strain (ϵ_c). The heterogeneity in rocks create spatially uneven strain response to the applied stress, which causes irregular fluctuations in the strain distribution from the specimen scale to pixel scale. To accurately measure the critical limit of tensile strain the analysis was performed at both the specimen-scale and pixel-scale (Figure 4).

At the specimen-scale, Stacey(1981) strain criterion was used to evaluate the critical threshold value of the tensile strain. It has been established that the initiation of extensile microcracks in rocks is highlighted by the deviation in the slope of vertical strain (ϵ_{yy}) vs. lateral strain (ϵ_{xx}) plot from linear to non-linear. Figure 4a shows the plot of vertical strain vs. lateral strain for BG-3 in which the change in the slope can be observed corresponding to -2.4e-4 strain value. Therefore, the critical tensile strain limit (ϵ_c) at the specimen scale was estimated as -2.4e-4 (negative strain(-) represents extension). Since the DIC strain measurements are based on pixel-scale, the critical limit of tensile strain needs to be calculated at the pixel-scale. At the pixel-scale, the value of ϵ_c was calculated based on CI stress threshold obtained through AE and was considered as 40% of the UCS. The 2nd, 10th and 20th percentiles of strain distribution were plotted as a function of the normalized stress (Figure 4b) for BG-3. The second percentile of the strain distribution was chosen for the evaluation of CI threshold because of the following two reasons: (i) the strain distribution for second percentile followed a trend similar to the evolution of the acoustic emission (Eberhardt et al., 1998; Moradian et al., 2016; Shirole et al., 2019), and (ii) at CI stress level, very few tensile cracks were formed, which signifies that very few pixels have tensile strain value greater than the critical limit. As shown in Figure 4b, the pixel-scale value of the critical tensile strain limit was estimated as -18e-4. After the evaluation of the critical limit of the tensile strain (ϵ_c), the nonelastic apparent tensile strain (ϵ_{AT}^{NT}) was determined as follows:

$$\epsilon_{AT}^{NE} = \left| \sum_{i=1}^{N} \langle \epsilon_{22,i} \rangle \right|, \text{where } \epsilon_{22,i} \leq \epsilon_c \tag{6}$$

The nonelastic apparent tensile strain component obtained through the above procedure was further utilized as a strain metrics to quantify the tensile deformations in the ROI region and to explicitly evaluate the extent of damage with the evolution of tensile cracks observed through the moment tensor analysis.

3.1.4 Crack Damage (CD) using Shear Strain Measurements

The nonelastic component of apparent shear strain was obtained using an approach similar to the quantification of the nonelastic apparent tensile strain component. As shear yield usually takes place along the plane of maximum shear strain (γ_{max}) (Jian-po et al., 2015; Shirole, Hedayat, & Walton, 2020), therefore maximum shear strain measurements were considered in this study for shear damage characterization. Figure 5 shows the maximum shear strain distribution at different levels of stress in the ROI. It is evident from the figure that as the stress on the rock specimen increases, the histogram shifts towards the right which indicates the increasing magnitude of the maximum shear strain. An increase in the heterogeneity of the maximum shear strain field can be observed at higher levels of stress which is consistent with the fact that shear cracking in rock dominates only beyond the crack damage (CD).

$$\gamma_{max} = \left| (\epsilon_{11} - \epsilon_{22})/2 \right| \tag{7}$$

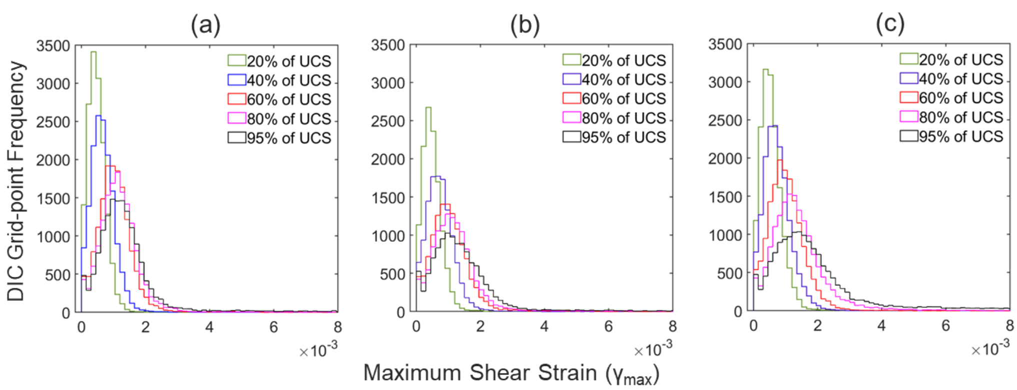

Figure 5. Histograms showing the maximum shear strain distribution in the ROI for three prismatic Barre granite specimens: (a) BG-1,(b) BG-2,(c) BG-3.

In this study, the damage due to tension has been characterized at pixel-scale measurements obtained through DIC. For the quantification of shear damage in the ROI, the non-elastic shear strain component needs to be evaluated at the pixel-scale. To estimate the pixel-scale non-elastic shear strain component, a critical threshold value of shear strain (γ_c) has been evaluated. As shear cracking in rocks primarily takes place beyond the CD stress level, therefore the rock specimen is expected to have less number of shear cracks as obtained through AE observations (Shirole, Hedayat, & Walton, 2020). Therefore, it is expected that at CD, very few pixels exhibit values of γ_{max} greater than γ_c. This shows that the critical shear strain limit (γ_c) should correspond to a small maximum shear strain (γ_{max}) distribution percentile. Figure 6 explains the procedure adopted for the determination of γ_c. The appropriate percentile distribution was chosen based on the fact that since shear cracking in rocks accelerates beyond CD stress level, the γ_{max} percentile corresponding to γ_c should show a deviation from linearity beyond CD threshold. To determine the value of γ_c, several percentiles of γ_{max} were plotted as a function of normalized stress (Figure 6). The strain distribution in the ROI follows a linear trend upto a certain stress level and then deviates at higher magnitudes of stress ($\sim$ 80% of the failure stress and above) which is consistent with the AE observations as shown in figure (2) for the rock specimen BG-3. Figure 6 shows that the data deviates from the linear trend at $\sim$ 80% of the UCS and above. This deviation from linearity can be associated with the unstable growth of the microcracks (Moradian et al., 2016). The 5^{th} percentile of the γ_{max} strain variation does not show any significant change in the slope, but the 0.5^{th} percentile and 0.1^{st} percentile showed a distinct deviation from linearity at around 80% of the failure stress. The 0.5^{th} percentile strain-field was chosen for the evaluation of (γ_c) because of two reasons (i) it followed a trend similar to the AE observations, (ii) it is consistent with the findings of the numerical model for granitic rocks proposed by (Sinha et al., 2020) which states that 0.3% -0.5% of grains in the micro-mechanical model showed shear damage at CD.

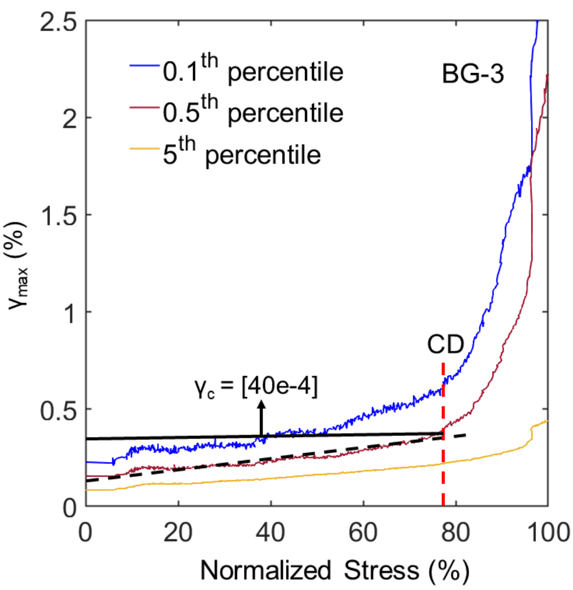

Figure 6. Procedure followed to obtain the pixel-scale critical shear strain limit (γ_c). The critical limit for maximum shear strain was obtained as (40e-4) corresponding to the 0.5^{th} percentile of the maximum shear strain variation (Shirole, Hedayat, & Walton, 2020)

The critical limit of the maximum shear strain (γ_c) obtained through the above procedure was (40e-4), which is greater than the critical limit of the tensile strain ($\epsilon_c = -18e - 5$) and also consistent with the previous observations that damage in brittle rocks initiate in tension prior to shear (M. Diederichs et al., 2004). These observations are also consistent with the CWFS (cohesion weakening and frictional strengthening) model proposed by Hajiabdolmajid et al. (2002). After the determination of the specific γ_c, procedure similar to the quantification of tensile damage was adopted to evaluate the total apparent shear strain and the non-elastic component of shear strain as shown in equation 8 and 9. The strain described in the above sections are considered as the apparent one, because in some cases it does not hold true due to the evolution of damage (Song et al., 2013)

$$\gamma_{AS}^{T} = \left| \sum_{i=1}^{N} \gamma_{max},_{i} \right| \tag{8}$$

$$\gamma_{AS}^{NE} = \left| \sum_{=1}^{N} \langle \gamma_{max},_{i} \rangle \right|, \text{, where } \gamma_{max},_{i} \geq \gamma_c \tag{9}$$

In equation 8 and 9, γ_{max} represents the maximum shear strain across the ROI at the N number of DIC grid points which in this case is 15770. Therefore, the apparent maximum shear strain can be defined as the summation of the maximum shear strain across the specified region of interest. The non-elastic component is evaluated by considering the maximum shear strain greater than the estimated critical value at the DIC grid points.

3.2 Crack Source Mechanisms

As discussed in the previous section that the progression of tensile and shear damage in rocks can be better understood on the basis of the non-elastic component of tensile and shear strain measurements. Therefore this section deals with the spatiotemporal distribution of the different crack source mechanism obtained through the 2D-DIC and AE techniques and their correlation.

Scholz (1968) (Scholz, 1968) reported that AE signals recorded during a rock fracture experiment, shows a rate of occurrence that can be correlated with the nonelastic stress-strain behavior of the rock. He conducted experiments on Westerly granite under unconfined compression and correlated the inelastic volumetric strain with the rate of AE, however the mechanism of cracking was not discussed in the study. A similar technique has been applied in this study where the occurrence of AE events were correlated with the DIC strain measurements with a major emphasis on the cracking mechanism. In particular, the evolution of different crack types obtained through moment tensor analysis were observed with increasing levels of nonelastic strain components (tensile and shear). Understanding this behavior is important to observe the extent of shear and tensile deformation in the rock specimen throughout the damage. With this in mind, the evolution of tensile and shear cracks and the calculated non-elastic component of tensile and shear strain has been plotted as a function of loading in the ROI for each rock specimen (Figure 7). The detailed description is provided in the following subsections.

3.2.1 Temporal Evolution of Crack Mechanisms

Figure 7a shows a consistent relationship between the evolution of the tensile cracks detected by AE and the non-elastic component of tensile strain detected by DIC, throughout the loading for all the three rock specimen. In uniaxial compression test, the CI threshold denotes the initiation of microcracks (also obtained from AE) in the form of stable extensile microcracks governed by the non-elastic tensile deformation in rocks (Lockner, 1993). This is quite evident from Figure 7a which shows a rise in the evolution of the tensile cracks in the CI region. The nonelastic tensile strain component which is a metric of damage around the flaw tips, also shows a significant rise around 30-40% of UCS. However, the rise in the AE crack mechanism occurred earlier than the strain values, this can be due to the fact that the DIC is related only to the surface strain measurements, whereas AE accounts for the deformation in the rock volume.

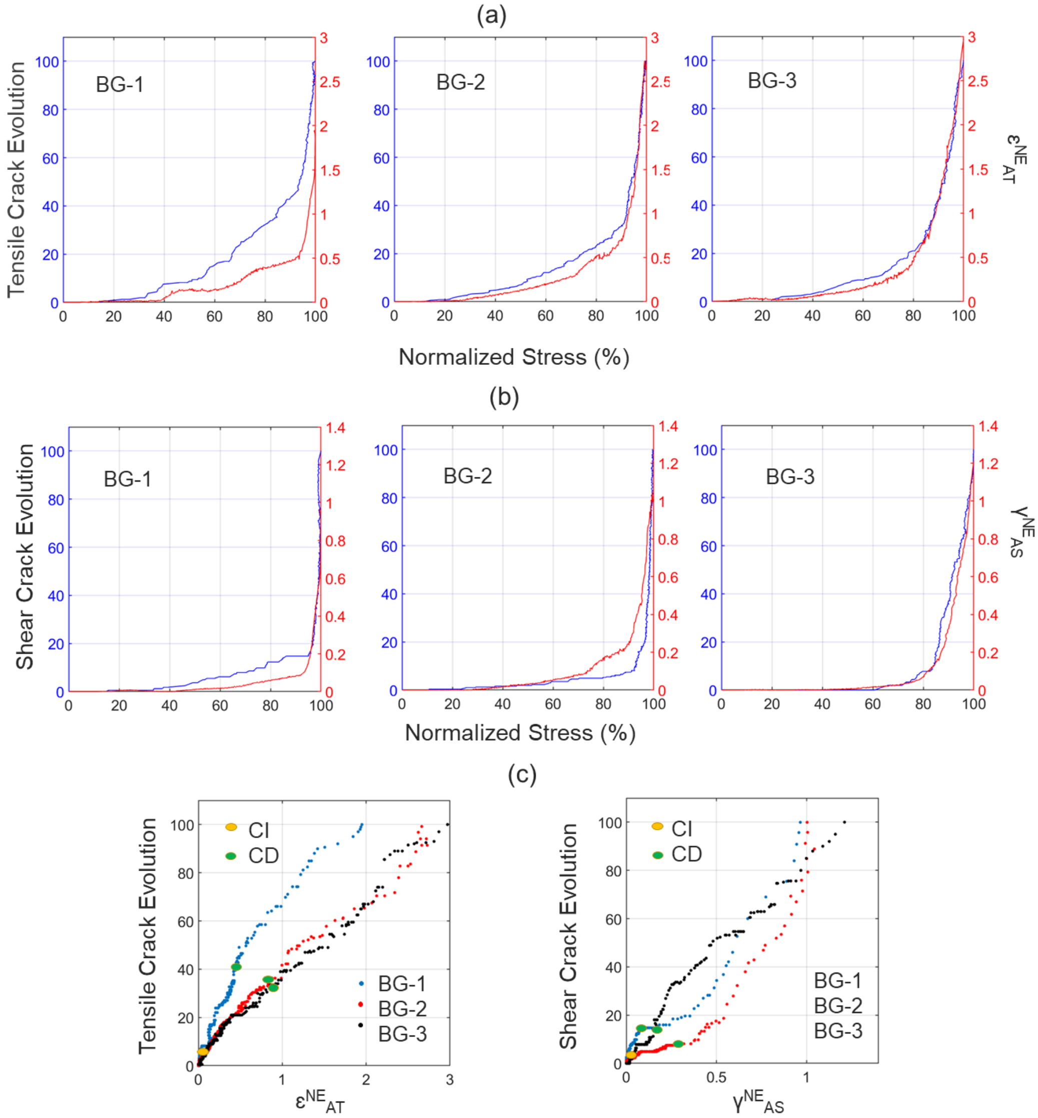

Figure 7. (a) Variation of tensile crack evolution (AE) and Non-elastic component of tensile strain (DIC) in the ROI for three Barre granite specimens, (b) Variation of shear crack evolution (AE) and Non-elastic component of maximum shear strain (DIC) in the ROI for three Barre granite specimens, (c) Correlation between the type of crack and nonelastic strain component in the ROI for the three rock specimens, the CI and CD has been distinguished by the yellow and green circles on the map.

When the load is increased further (from CI to CD), the nonelastic tensile strain increases with the increasing number of tensile cracks. The curve shows an accelerated increase in the nonelastic tensile strain around the CD region (80%-90% of UCS) which is consistent with the fact that the damage in brittle rocks primarily occur due to the local tensile stresses even if the rocks are subjected to compressive stress field. From these observations, it can be concluded that the nonelastic component of the tensile strain is a good representative of the tensile crack evolution in the rock specimen and it can be used to quantify the initiation, growth and coalescence of the extensile microcracking in rocks. Figure 7c shows the correlation between the cumulative number of tensile cracks and non-elastic tensile strain component evaluated through DIC full-field strain measurements in the ROI. In particular, a near linear correlation can be seen between the tensile crack and non-elastic tensile strain field. At higher levels of stress the trend becomes non-linear because of the loss in correlation of strain measurements. This observation is consistent with the findings of many direct microscopic observational approaches (e.g. optical microscope, scanning electron microscopy (SEM) etc.) which indicate that crack initiation takes place in tensile mode at the flaw tips at early stages of loading in the rock specimen.

Since the nonelastic apparent maximum shear strain (γ_{AS}^{NE}) can be used as a metric for the characterization of shear damage in rocks, the evolution of shear cracks and the nonelastic component of maximum shear strain was plotted as a function of normalized stress for the three rock specimen in the ROI (Figure 7b). The curves show a sharp increase around the CD threshold ($80\% - 90\%$) and above. These observations are consistent with many experimental and numerical evaluation which states that the microcracks induced by the tensile strain begin to coalesce beyond the CD stress threshold and causes the shear-strain induced microcracks to dominate (M. Diederichs, 2003; M. Diederichs et al., 2004; J. Peng et al., 2017). These results also indicate that shear strain at the pixel scale represents a more local level of shear damage and thus can be correlated with the AE crack mechanism. A similar observation can be seen in figure 7c, which shows the ratio of the shear cracks with respect to total number of shear cracks at each stress level as a function of nonelastic maximum shear strain. The trend shows a near linear correlation, although the number of shear cracks between the CI and CD limit is very low. After the CD, an increase in the number of shear cracks can be seen.

The results in the present study shows that with the evolution of shear cracks, the nonelastic component of shear strain increases by seven to ninefolds from the CD limit to the failure of the specimen. These observations are consistent with the conclusions of several other studies such as Martin and Chandler (1994), Diederichs et al.(2003), Martin et al. (2010), Sinha and Walton (2020) and the CWFS (cohesion weakening and frictional strengthening) model proposed by Hajiabdolmajid et al. (2002).

The consistent correlation between the temporal evolution of tensile and shear cracks with the nonelastic DIC strain components provides a better understanding about the mechanism of microfracture accumulation and failure in brittle rocks. The results suggest that the formation of macrocrack involves the existence of both tensile and shear microcracks but the proportion of their evolution is different as the damage progresses. As shown in figure 7a the evolution of tensile microcracks and nonelastic tensile strain shows an increasing trend between the CI and CD which can be associated with the tensile opening at the macroscale. Once the tensile cracking has occured at the macroscale, the ratio of shear crack and nonelastic shear strain dominates (beyond CD) this could be due to the separation caused by the tensile opening in the rock specimen. Thus, the increasing trend in the evolution of shear cracks (from CD to the failure of the rock specimen) can be interpreted as the shear macrocrack formation. Although few shear microcracks can be observed between the CI and CD (figure 7b) this can be interpreted as the widening of the fracture process zone (L. N. Y. Wong & Xiong, 2018). In addition to this, the present experimental results also confirms explicitly an interesting finding that the strain metrics applied in the present study can be used as an effective tool to identify the various cracking levels in rock damage in combination with the AE monitoring.

3.2.2 Spatial Distribution of Crack Mechanisms

The evolution of the mode of fracture through AE was obtained using the moment tensor inversion technique. In order to analyze the mode of deformation from DIC strain measurements, the normal and shear component of strain were calculated by adopting a procedure similar to the method proposed by Tal et al. (2016). To analyze the strain in the ROI, the principal strain component was calculated for all the grid points in the specific region (ROI). In order to get the damage features (microcracks), only those grid points in the ROI were selected in which the difference between the principal strain component was larger than 0.01 (1%) (Tal et al., 2016) and where more than 5 grid points remained (filter size is 5, strain resolution of DIC was $2250\mu\epsilon$). This filtering of the strain map was done to eliminate the noise with a conservative approach so as to ensure that the damage features obtained through the image based strain profiles after filtering had minimum measurement errors. These damage features were considered as the microcracks and their orientation was obtained through visual inspection. Once the orientation was identified, the normal and shear components of the strains were calculated by resolving the values perpendicular and parallel to the crack trend. Observations from the two techniques, that is the evolution of the tensile and shear cracks through moment tensors of AE and the mode of deformation obtained through image based strain profiles from DIC were plotted at different levels of stress. Figures 8 and 9 shows the spatial distribution of the AE cracks obtained through the moment tensor analysis and the normal and shear component of the strain obtained through DIC in the ROI for BG-3. The evolution of tensile crack is compared with the normal component of strain (Figure 8) and the shear crack evolution is compared with the shear component of strain along the crack trend (Figure 9).

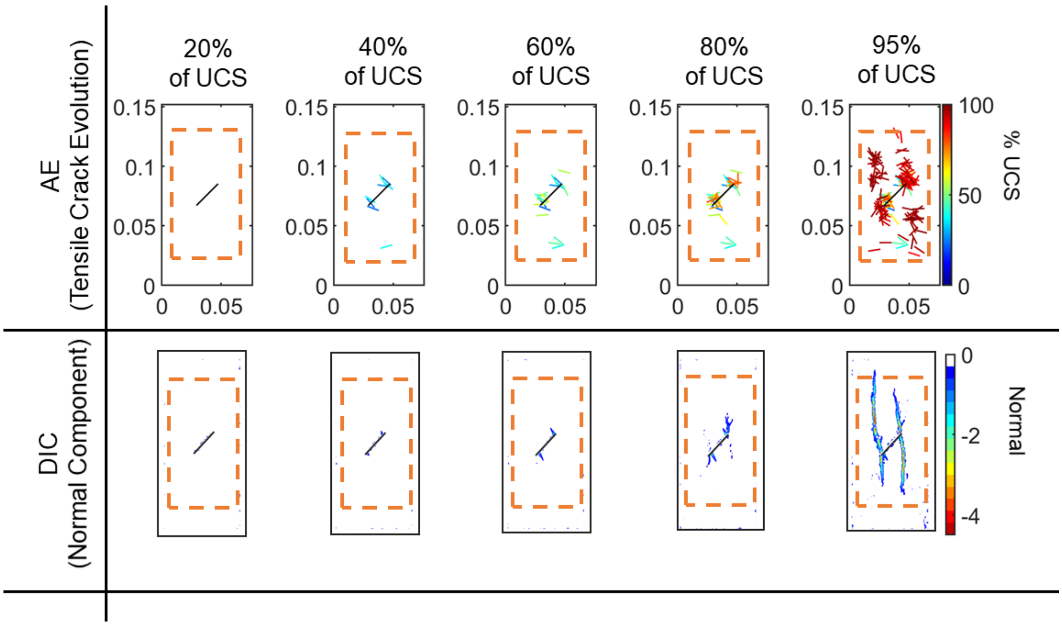

Figure 8. Comparison between the mode of deformation obtained through AE (tensile cracks) and DIC (normal component of strain) at different levels of stress in the ROI for BG-3.

Figure 8 shows that the tensile cracks initiated close to the flaw tips at around 40% of UCS which is the CI for BG-3. At the same stress level, the normal mode of deformation can also be seen in the strain maps. Few microcracks through AE can be seen in the lower region of the specimen which is not evident in the DIC strain maps, this could be due to the damage along the depth of the specimen which cannot be observed in the image analysis. Moreover,

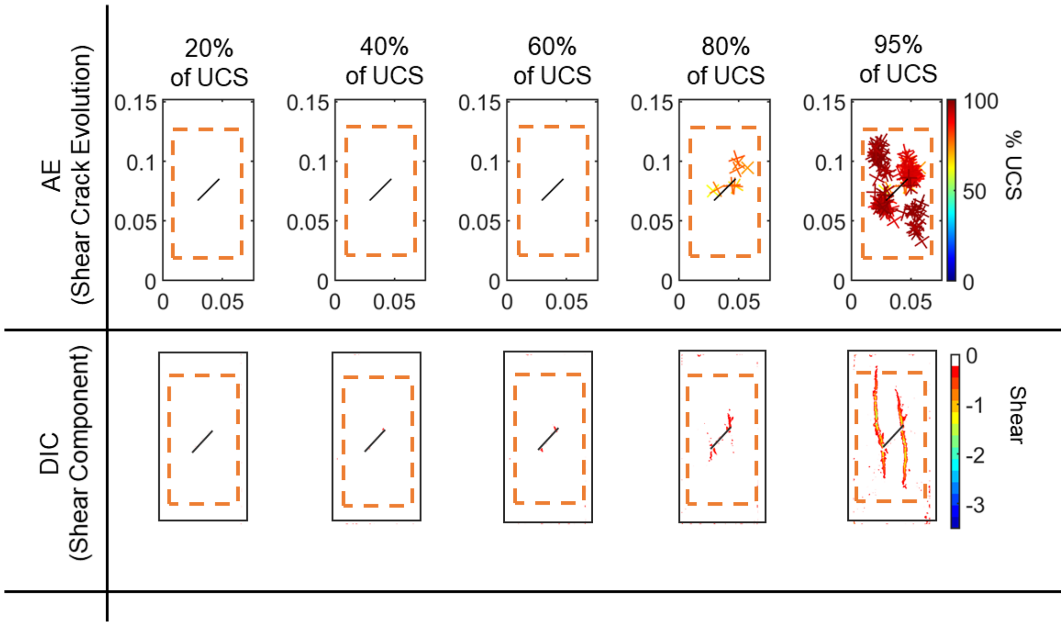

Figure 9. Comparison between the mode of deformation obtained through AE (shear cracks) and DIC (shear component of strain) at different levels of stress in the ROI for BG-3

as the loading increases, the microcracks propagate subparallel along the direction of the major principal stress. As expected, the strain concentration at the flaw tips increases with increasing levels of stress.

Figure 9 shows the evolution of the shear cracks from the AE moment tensor analysis and the shear component of strain resolved parallel to the crack trend at different levels of stress for BG-3. At initial stages (40-50% of the failure stress) no shear cracking can be seen through both the techniques. The shear cracks initiated at higher levels of stress (60-80% of the failure stress), which is very close to the CD stress threshold of the rock specimen. The evolution of shear microcracks between the CI and CD is associated with the widening of the fracture process zone. Similarly, some shear strain concentration can be seen at 60% of the failure stress which can be due to the evolution of few shear microcracks in between CI to CD. The results of the shear component of strain measurements are very consistent with the shear crack evolution at later stages of loading. Near failure (95% of UCS) both modes of deformation (tensile and shear) was observed, but the shear mode is more dominant.

These observations experimentally illustrate the relationship between the mode of deformation obtained through image based strain profiles and the process of microfracturing obtained through the moment tensors of AE. The results are consistent with the previous observations (Tapponnier & Brace, 1976; Paterson & Wong, 2005) that showed that microcracks initiate in tension in low porosity brittle rocks further extending to shear damage. Although it has been previously observed that the nonelastic strain component shows a consistent relationship with the tensile and shear damage in rocks, these results further confirms that the overall deformation in rocks subjected to various levels of stress is a combination of both (normal and shear) modes of deformation.

4 Conclusions

In this study, the temporal-spatial evolution of stress-induced microcracks and the proportion of different modes of cracking around the flaw tip was studied for Barre granite specimen with an existing flaw under unconfined compression. The moment tensor analysis was employed on the AE waveforms for the evaluation of the crack mechanism in rocks subjected to unconfined compression and the non-elastic tensile and shear strain component was computed from the 2D-DIC strain measurements. Based on the results from the previous studies that AE represents the inelastic deformation (microcracking) in the rocks, the damage mechanism obtained through AE was linked with the non-elastic tensile and shear strain field evaluated from the DIC strain monitoring.

The 2D-DIC strain maps showed that as the load increases the heterogeneity in the strain field increases due to the accumulated damage in the rock microstructure. Based on the fact that the damage process in rocks initiate in tension, the tensile strain distribution was analyzed in the ROI. Similarly, to analyze the evolution of shear cracks, the distribution of shear strain was observed through the maximum apparent shear strain in the ROI. In particular, the nonelastic tensile strain (ϵ_{AT}^{NE}) and the nonelastic shear strain (γ_{AS}^{NE}) distribution was analyzed in the specific region of interest. To obtain the non-elastic component of strains, the critical limit for tensile (ϵ_c) and shear strain (γ_c) were computed above which the strain was considered as non-elastic. The results showed that the evolution of tensile cracks obtained through the moment tensor analysis and the non-elastic apparent tensile strain followed a consistent trend throughout the loading for all the experiments. Similar observation was seen for the evolution of shear cracks and non-elastic shear strain.

To analyze the mode of deformation from the DIC based strain profiles, the normal and shear components of strain along the damage features were computed. Using filtering techniques to the 2D-DIC strain data, linear damage features (microcracks) and their orientation were obtained from the image based strain profiles. Once the linear features and their orientation was identified, the strain field was resolved into the normal and shear components along the crack length. The study showed a consistent trend between the AE and DIC observations in the ROI for the shear and normal deformations. In particular, tensile deformation was observed throughout the loading initiating from the CI stress threshold while shear deformation dominated closer to the peak stress.

ACKNOWLEDGMENTS

This research is supported by the U.S.Department of Energy, Office of Basic Energy Sciences, under Award Number DE-SC0019117. Interested readers can obtain the data related to this research article from https://figshare.com/s/56776f9041c56a3f29bc.

References

Bazant, Z. P., & Kazemi, M. (1990). Determination of fracture energy, process zone length and brittleness number from size effect, with application to rock and conerete. *International Journal of fracture*, *44*(2), 111–131.

Bieniawski, Z. (1967). Mechanism of brittle fracture of rock: part ii—experimental studies. In *International journal of rock mechanics and mining sciences & geomechanics abstracts* (Vol. 4, pp. 407–423).

Bieniawski, Z. T. (1967). Mechanism of brittle fracture of rock: part i—theory of the fracture process. In *International journal of rock mechanics and mining sciences & geomechanics abstracts* (Vol. 4, pp. 395–406).

Bourcier, M., Bornert, M., Dimanov, A., Héripré, E., & Raphanel, J. (2013). Multiscale experimental investigation of crystal plasticity and grain boundary sliding in synthetic halite using digital image correlation. *Journal of Geophysical Research: solid earth*, *118*(2), 511–526.

Brace, W., Paulding Jr, B., & Scholz, C. (1966). Dilatancy in the fracture of crystalline rocks. *Journal of Geophysical Research*, *71*(16), 3939–3953.

Bruck, H., McNeill, S., Sutton, M. A., & Peters, W. (1989). Digital image correlation using newton-raphson method of partial differential correction. *Experimental mechanics*, *29*(3), 261–267.

Chang, S.-H., & Lee, C.-I. (2004). Estimation of cracking and damage mechanisms in rock under triaxial compression by moment tensor analysis of acoustic emission. *International Journal of Rock Mechanics and Mining Sciences*, *41*(7), 1069–1086.

Cheng, J.-L., Yang, S.-Q., Chen, K., Ma, D., Li, F.-Y., & Wang, L.-M. (2017). Uniaxial experimental study of the acoustic emission and deformation behavior of composite rock based on 3d digital image correlation (dic). *Acta Mechanica Sinica*, *33*(6), 999–1021.

Cheng, Y., & Wong, L. N. Y. (2018). Microscopic characterization of tensile and shear fracturing in progressive failure in marble. *Journal of Geophysical Research: Solid Earth*, *123*(1), 204–225.

Crider, J. G. (2015). The initiation of brittle faults in crystalline rock. *Journal of Structural Geology*, *77*, 159–174.

Dai, F., & Xia, K. (2010). Loading rate dependence of tensile strength anisotropy of barre granite. *Pure and applied geophysics*, *167*(11), 1419–1432.

Diederichs, M. (2003). Manuel rocha medal recipient rock fracture and collapse under low confinement conditions. *Rock Mechanics and Rock Engineering*, *36*(5), 339–381.

Diederichs, M., Kaiser, P., & Eberhardt, E. (2004). Damage initiation and propagation in hard rock during tunnelling and the influence of near-face stress rotation. *International Journal of Rock Mechanics and Mining Sciences*, *41*(5), 785–812.

Diederichs, M. S. (1999). *Instability of hard rockmasses, the role of tensile damage and relaxation* (Unpublished doctoral dissertation). University of Waterloo.

Dong, W., Wu, Z., Zhou, X., Wang, N., & Kastiukas, G. (2017). An experimental study on crack propagation at rock-concrete interface using digital image correlation technique. *Engineering fracture mechanics*, *171*, 50–63.

Eberhardt, E., Stead, D., Stimpson, B., & Read, R. (1998). Identifying crack initiation and propagation thresholds in brittle rock. *Canadian geotechnical journal*, *35*(2), 222–233.

Eberhardt, E., Stimpson, B., & Stead, D. (1999). Effects of grain size on the initiation and propagation thresholds of stress-induced brittle fractures. *Rock mechanics and rock engineering*, *32*(2), 81–99.

Fortin, J., Stanchits, S., Dresen, G., & Gueguen, Y. (2009). Acoustic emissions monitoring during inelastic deformation of porous sandstone: comparison of three modes of deformation. *Pure and Applied Geophysics*, *166*(5-7), 823–841.

Fredrich, J. T., Evans, B., & Wong, T.-F. (1989). Micromechanics of the brittle to plastic transition in carrara marble. *Journal of Geophysical Research: Solid Earth*, *94*(B4), 4129–4145.

Ghamgosar, M., Erarslan, N., & Williams, D. (2017). Experimental investigation of fracture process zone in rocks damaged under cyclic loadings. *Experimental Mechanics*, *57*(1), 97–113.

Goldsmith, W., Sackman, J., & Ewerts, C. (1976). Static and dynamic fracture strength of barre granite. In *International journal of rock mechanics and mining sciences & geomechanics abstracts* (Vol. 13, pp. 303–309).

Graham, C. C., Stanchits, S., Main, I. G., & Dresen, G. (2010). Comparison of polarity and moment tensor inversion methods for source analysis of acoustic emission data. *International journal of rock mechanics and mining sciences (Oxford, England: 1997)*, *47*(1), 161.

Griffith, A. A. (1921). Vi. the phenomena of rupture and flow in solids. *Philosophical transactions of the royal society of london. Series A, containing papers of a mathematical or physical character*, *221*(582-593), 163–198.

Guo, M., Alam, S. Y., Bendimerad, A. Z., Grondin, F., Rozière, E., & Loukili, A. (2017). Fracture process zone characteristics and identification of the micro-fracture phases in recycled concrete. *Engineering Fracture Mechanics*, *181*, 101–115.

Hajiabdolmajid, V., Kaiser, P. K., & Martin, C. (2002). Modelling brittle failure of rock. *International Journal of Rock Mechanics and Mining Sciences*, *39*(6), 731–741.

Hallbauer, D., Wagner, H., & Cook, N. (1973). Some observations concerning the microscopic and mechanical behaviour of quartzite specimens in stiff, triaxial compression tests. In *International journal of rock mechanics and mining sciences & geomechanics abstracts* (Vol. 10, pp. 713–726).

Hampton, J., Gutierrez, M., Matzar, L., Hu, D., & Frash, L. (2018). Acoustic emission characterization of microcracking in laboratory-scale hydraulic fracturing tests. *Journal of Rock Mechanics and Geotechnical Engineering*, *10*(5), 805–817.

Hedayat, A., Pyrak-Nolte, L. J., & Bobet, A. (2014). Detection and quantification of slip along non-uniform frictional discontinuities using digital image correlation. *Geotechnical Testing Journal*, *37*(5), 786–799.

Hedayat, A., & Walton, G. (2017). Laboratory determination of rock fracture shear stiffness using seismic wave propagation and digital image correlation. *Geotechnical Testing Journal*, *40*(1), 92–106.

Iqbal, M., & Mohanty, B. (2007). Experimental calibration of isrm suggested fracture toughness measurement techniques in selected brittle rocks. *Rock Mechanics and Rock Engineering*, *40*(5), 453.

Jian-po, L., Yuan-hui, L., Shi-da, X., Shuai, X., & Chang-yu, J. (2015). Cracking mechanisms in granite rocks subjected to uniaxial compression by moment tensor analysis of acoustic emission. *Theoretical and Applied Fracture Mechanics*, *75*, 151–159.

Kao, C.-S., Tarokh, A., Biolzi, L., & Labuz, J. F. (2016). Inelastic strain and damage in surface instability tests. *Rock Mechanics and Rock Engineering*, *49*(2), 401–415.

Kim, J.-S., Lee, K.-S., Cho, W.-J., Choi, H.-J., & Cho, G.-C. (2015). A comparative evaluation of stress–strain and acoustic emission methods for quantitative damage assessments of brittle rock. *Rock Mechanics and Rock Engineering*, *48*(2), 495–508.

Kranz, R. L. (1979). Crack growth and development during creep of barre granite. In *International journal of rock mechanics and mining sciences & geomechanics abstracts* (Vol. 16, pp. 23–35).

Kranz, R. L. (1983). Microcracks in rocks: a review. *Tectonophysics*, *100*(1-3), 449–480.

Kurz, J. H., Grosse, C. U., & Reinhardt, H.-W. (2005). Strategies for reliable automatic onset time picking of acoustic emissions and of ultrasound signals in concrete. *Ultrasonics*, *43*(7), 538–546.

Lajtai, E. (1974). Brittle fracture in compression. *International Journal of Fracture*, *10*(4), 525–536.

Li, B. Q., da Silva, B. G., & Einstein, H. (2019). Laboratory hydraulic fracturing of granite: acoustic emission observations and interpretation. *Engineering Fracture Mechanics*, *209*, 200–220.

Li, B. Q., & Einstein, H. H. (2017). Comparison of visual and acoustic emission observations in a four point bending experiment on barre granite. *Rock Mechanics and Rock Engineering*, *50*(9), 2277–2296.

Lin, Q., & Labuz, J. F. (2013). Fracture of sandstone characterized by digital image correlation. *International Journal of Rock Mechanics and Mining Sciences*, *60*, 235–245.

Lin, Q., Wan, B., Wang, Y., Lu, Y., & Labuz, J. F. (2019). Unifying acoustic emission and digital imaging observations of quasi-brittle fracture. *Theoretical and Applied Fracture Mechanics*, *103*, 102301.

Lin, Q., Yuan, H., Biolzi, L., & Labuz, J. F. (2014). Opening and mixed mode fracture processes in a quasi-brittle material via digital imaging. *Engineering Fracture Mechanics*, *131*, 176–193.

Lockner, D. (1993). The role of acoustic emission in the study of rock fracture. In *International journal of rock mechanics and mining sciences & geomechanics abstracts* (Vol. 30, pp. 883–899).

Maeda, N. (1985). A method for reading and checking phase times in autoprocessing system of seismic wave data. *Zisin*, *38*, 365–379.

Martin, C., & Chandler, N. (1994). The progressive fracture of lac du bonnet granite. In *International journal of rock mechanics and mining sciences & geomechanics abstracts* (Vol. 31, pp. 643–659).

McClintock, F. A., & Irwin, G. (1965). Plasticity aspects of fracture mechanics. In *Fracture toughness testing and its applications.* ASTM International.

Modiriasari, A., Bobet, A., & Pyrak-Nolte, L. J. (2017). Active seismic monitoring of crack initiation, propagation, and coalescence in rock. *Rock Mechanics and Rock Engineering*, *50*(9), 2311–2325.

Moore, D. E., & Lockner, D. (1995). The role of microcracking in shear-fracture propagation in granite. *Journal of Structural Geology*, *17*(1), 95–114.

Moradian, Z., Einstein, H. H., & Ballivy, G. (2016). Detection of cracking levels in brittle rocks by parametric analysis of the acoustic emission signals. *Rock Mechanics and Rock Engineering*, *49*(3), 785–800.

Morgan, S. P., Johnson, C. A., & Einstein, H. H. (2013). Cracking processes in barre granite: fracture process zones and crack coalescence. *International Journal of Fracture*, *180*(2), 177–204.

Nasseri, M., Grasselli, G., & Mohanty, B. (2010). Fracture toughness and fracture roughness in anisotropic granitic rocks. *Rock Mechanics and Rock Engineering*, *43*(4), 403–415.

Nicksiar, M., & Martin, C. (2012). Evaluation of methods for determining crack initiation in compression tests on low-porosity rocks. *Rock Mechanics and Rock Engineering*, *45*(4), 607–617.

Nicksiar, M., & Martin, C. (2013). Crack initiation stress in low porosity crystalline and sedimentary rocks. *Engineering Geology*, *154*, 64–76.

Ohtsu, M. (1991). Simplified moment tensor analysis and unified decomposition of acoustic emission source: application to in situ hydrofracturing test. *Journal of Geophysical Research: Solid Earth*, *96*(B4), 6211–6221.

Ohtsu, M. (1995). Acoustic emission theory for moment tensor analysis. *Research in Nondestructive Evaluation*, *6*(3), 169–184.

Pan, B., Qian, K., Xie, H., & Asundi, A. (2009). Two-dimensional digital image correlation for in-plane displacement and strain measurement: a review. *Measurement science and technology*, *20*(6), 062001.

Paterson, M. S., & Wong, T.-f. (2005). *Experimental rock deformation-the brittle field.* Springer Science & Business Media.

Peng, J., Wong, L. N. Y., & Teh, C. I. (2017). Influence of grain size heterogeneity on strength and microcracking behavior of crystalline rocks. *Journal of Geophysical Research: Solid Earth*, *122*(2), 1054–1073.

Peng, S., & Johnson, A. (1972). Crack growth and faulting in cylindrical specimens of chelmsford granite. In *International journal of rock mechanics and mining sciences & geomechanics abstracts* (Vol. 9, pp. 37–86).

Peng, S. S. (1975). A note on the fracture propagation and time-dependent behavior of rocks in uniaxial tension. In *International journal of rock mechanics and mining sciences & geomechanics abstracts* (Vol. 12, pp. 125–127).

Pestman, B., & Van Munster, J. (1996). An acoustic emission study of damage development and stress-memory effects in sandstone. In *International journal of rock mechanics and mining sciences & geomechanics abstracts* (Vol. 33, pp. 585–593).

Reches, Z., & Lockner, D. A. (1994). Nucleation and growth of faults in brittle rocks. *Journal of Geophysical Research: Solid Earth*, *99*(B9), 18159–18173.

Richards, P. G., & Aki, K. (1980). *Quantitative seismology: Theory and methods.* Freeman.

Scholz, C. (1968). Microfracturing and the inelastic deformation of rock in compression. *Journal of Geophysical Research*, *73*(4), 1417–1432.

Schwartz, E., Saralaya, R., Cuadra, J., Hazeli, K., Vanniamparambil, P. A., Carmi, R., ... Kontsos, A. (2013). The use of digital image correlation for non-destructive and multi-scale damage quantification. In *Sensors and smart structures technologies for civil, mechanical, and aerospace systems 2013* (Vol. 8692, p. 86922H).

Shirole, D., Hedayat, A., & Walton, G. (2019). Experimental relationship between compressional wave attenuation and surface strains in brittle rock. *Journal of Geophysical Research: Solid Earth*, *124*(6), 5770–5793.

Shirole, D., Hedayat, A., & Walton, G. (2020). Illumination of damage in intact rocks by

ultrasonic transmission-reflection and digital image correlation. *Journal of Geophysical Research: Solid Earth*, *125*(7), e2020JB019526.
Shirole, D., Walton, G., & Hedayat, A. (2020). Experimental investigation of multi-scale strain-field heterogeneity in rocks. *International Journal of Rock Mechanics and Mining Sciences*, *127*, 104212.
Sinha, S., Shirole, D., & Walton, G. (2020). Investigation of the micromechanical damage process in a granitic rock using an inelastic bonded block model (bbm). *Journal of Geophysical Research: Solid Earth*, *125*(3), e2019JB018844.
Sondergeld, C., & Estey, L. (1982). Source mechanisms and microfracturing during uniaxial cycling of rock. *pure and applied geophysics*, *120*(1), 151–166.
Song, H., Zhang, H., Fu, D., Kang, Y., Huang, G., Qu, C., & Cai, Z. (2013). Experimental study on damage evolution of rock under uniform and concentrated loading conditions using digital image correlation. *Fatigue & Fracture of Engineering Materials & Structures*, *36*(8), 760–768.
Stacey, T. (1981). A simple extension strain criterion for fracture of brittle rock. In *International journal of rock mechanics and mining sciences & geomechanics abstracts* (Vol. 18, pp. 469–474).
Sutton, M. A., Orteu, J. J., & Schreier, H. (2009). *Image correlation for shape, motion and deformation measurements: basic concepts, theory and applications.* Springer Science & Business Media.
Tal, Y., Evans, B., & Mok, U. (2016). Direct observations of damage during unconfined brittle failure of carrara marble. *Journal of Geophysical Research: Solid Earth*, *121*(3), 1584–1609.
Tapponnier, P., & Brace, W. (1976). Development of stress-induced microcracks in westerly granite. In *International journal of rock mechanics and mining sciences & geomechanics abstracts* (Vol. 13, pp. 103–112).
Tarokh, A., Makhnenko, R. Y., Fakhimi, A., & Labuz, J. F. (2017). Scaling of the fracture process zone in rock. *International Journal of Fracture*, *204*(2), 191–204.
Wawersik, W., & Fairhurst, C. (1970). A study of brittle rock fracture in laboratory compression experiments. In *International journal of rock mechanics and mining sciences & geomechanics abstracts* (Vol. 7, pp. 561–575).
Wong, L., & Einstein, H. (2009). Crack coalescence in molded gypsum and carrara marble: part 2—microscopic observations and interpretation. *Rock Mechanics and Rock Engineering*, *42*(3), 513–545.
Wong, L. N. Y., & Xiong, Q. (2018). A method for multiscale interpretation of fracture processes in carrara marble specimen containing a single flaw under uniaxial compression. *Journal of Geophysical Research: Solid Earth*, *123*(8), 6459–6490.
Wulff, A.-M., Hashida, T., Watanabe, K., & Takahashi, H. (1999). Attenuation behaviour of tuffaceous sandstone and granite during microfracturing. *Geophysical Journal International*, *139*(2), 395–409.
Xu, X., & Zhang, Z.-Z. (2018). Acoustic emission and damage characteristics of granite subjected to high temperature. *Advances in Materials Science and Engineering*, *2018*.
Zafar, S., Hedayat, A., & Moradian, O. (2020). Evaluation of crack initiation and damage in intact barre granite rocks using acoustic emission. *Geotechnical Earthquake Engineering and Special Topics*.
Zhao, Y.-h., Huang, J.-f., & Wang, R. (1993). Real-time sem observations of the microfracturing process in rock during a compression test. In *International journal of rock mechanics and mining sciences & geomechanics abstracts* (Vol. 30, pp. 643–652).